

# The effects of TiB<sub>2</sub> on microstructure, mechanical properties, and fluidity of AlSi10MnMg alloy fabricated by high pressure die casting

Lei Liu<sup>a</sup>, Weixiao Yang<sup>a</sup>, Kai Zhao<sup>a</sup>, Yanqiang Li<sup>a</sup>, Tao Zhang<sup>c</sup>, Ying Fu<sup>d</sup>, Zhirou Zhang<sup>a</sup>, Enyu Guo<sup>a,b</sup>, Huijun Kang<sup>a,b</sup>, Zongning Chen<sup>a,b\*</sup>, Tongmin Wang<sup>a,b\*\*</sup>

- Key Laboratory of Solidification Control and Digital Preparation Technology (Liaoning Province), School of Materials Science and Engineering, Dalian University of Technology, Dalian 116024, China
  - 2. Ningbo Institute of Dalian University of Technology, Ningbo 315000, China
    - 3. Shenzhen Leadwell Technology Co., Ltd, Shenzhen 518110, China
  - 4. Songshan Lake Materials Laboratory, Dongguan, Guangdong, 523808, China

Abstract: Optimizing the mechanical properties and fluidity of hypoeutectic Al-Si alloys in high-pressure die casting (HPDC) is critical for manufacturing thin-walled components with large size. In this study, an AlSi10MnMg alloy was fabricated by using a fluidity mold with three channels of different thicknesses to investigate the influence of TiB2 on the microstructure, mechanical properties, and fluidity of the alloy during long-distance filling in HPDC. Results show that increasing the filling distance decreases the area fraction of externally solidified crystals (ESCs) and alloy density, while porosity volume and size increase. The addition of 0.3 wt.% Al-4Ti-2B significantly reduced ESCs and porosity contents, improving the filling distance from 1700 mm to 1833 mm. The reduction in ESCs in the castings by TiB2 is attributed to its ability to promote the migration of ESCs from the shot sleeve toward the melt center, where temperature and flow velocity are higher. At a filling distance of 1300 mm, the ultimate tensile strength (UTS), yield strength (YS), and elongation increased notably with addition of 0.3 wt.% Al-4Ti-2B. When the addition of Al-4Ti-2B was increased to 0.6 wt.%, the area fraction of ESCs in the channel increased compared to that with 0.3 wt.%, and the filling distance slightly decreased to 1796.9 mm. Mechanical performance with 0.6 wt.% was inferior at short distances but surpassed that of 0.3 wt.% at distances beyond 1000 mm. This work reveals the role of TiB2 in regulating solidification and flow during long-range filling, offering new insights into the processability of HPDC Al-Si alloys.

Keywords: high pressure die casting; TiB2; AlSi10MnMg; fluidity; porosity.

#### 1 Introductions

Due to its high efficiency, precision, and excellent thin-wall forming capability, high-pressure die casting (HPDC) is widely used for mass production of critical automotive components <sup>[1]</sup>. Hypoeutectic Al-Si alloys are the preferred materials for lightweight and multifunctional automotive parts due to their good fluidity, excellent castability, balanced strength and toughness, and low cost<sup>[2-4]</sup>. The increasing demand for energy efficiency requires thinner and more integrated body structural components while maintaining strength and torsional rigidity, leading to greater structural complexity in thin-walled parts<sup>[5]</sup>. The manufacture of large,

thin-walled castings with complex geometries imposes higher demands on the long-distance fluidity and mechanical stability of alloys in HPDC.

The coupled high-speed flow and rapid solidification in HPDC produce a heterogeneous microstructure in Al-Si alloys, consisting of a fine-grained surface layer, a central zone rich in externally solidified crystals (ESCs), and an intermediate eutectic band<sup>[6-8]</sup>. Gas entrapment and incomplete filling of the melt in the mold cavity can lead to casting defects such as porosity and shrinkage<sup>[9, 10]</sup>. The mechanical properties of HPDC parts depend on the heterogeneous solidification structure and porosity. Jiao et al.<sup>[11]</sup> reported that in low-porosity AlSi10MnMg alloys, cracks initiate mainly in the skin layer, whereas in

high-porosity alloys, crack propagation occurs via consolidation and collapse of pores. Fu et al.<sup>[12]</sup> found that in Al-6Si-Mg alloys cast with long filling distances, cracks originate from the ESC/eutectic Si interface in low-defect conditions, and from porosity in high-defect regions.

Melt fluidity is closely linked to solid phase evolution during filling, as the flow stops once a critical fraction of solid has formed. Han et al.[13] suggested that increasing solid content during HPDC causes a pressure drop in the cavity, and filling ceases when the resistance equals the driving pressure. The resistance of semi-solid melt to flow depends on solid fraction and grain size, with resistance rising rapidly once the solid fraction reaches a critical value, and smaller grains reducing shear resistance [14, 15]. Therefore, understanding the coupled behavior of solidification and flow is essential for modifying microstructure, defect, and fluidity in HPDC alloys. Extensive efforts have been made to improve the mechanical properties and fluidity of HPDC Al-Si alloys through alloy composition<sup>[16-18]</sup>, slow shot speeds<sup>[19]</sup>, fast shot speeds<sup>[20]</sup>, casting temperature<sup>[21, 22]</sup>, and vacuum assistance<sup>[23]</sup>. However, to meet the demands of casting ultra-large and complex thin-walled parts, additional strategies are needed to further enhance the formability and performance of HPDC Al-Si alloys.

Al-Ti-B is a widely used and cost-effective grain refiner under gravity casting conditions, aimed at improving as-cast microstructure, reducing defects, and enhancing mechanical properties<sup>[24, 25]</sup>. The grain refinement effect of Al-Ti-B stems heterogeneous nucleation of α-Al promoted by TiB<sub>2</sub> particles in the presence of free Ti atoms, and this effect is strongly influenced by alloy composition and cooling rate<sup>[26]</sup>. The refinement provided by Al-Ti-B also contributes to enhanced melt fluidity under gravity casting conditions. Dahle et al.[27] demonstrated through spiral flow tests that the addition of grain refiners improves the fluidity of AlSi7Mg and AlSi11Mg alloys when the Ti content exceeds 0.12%, while lower additions reduce flowability. The alloy refined with 0.015% B exhibited the finest grains and the best fluidity. Zhao et al.<sup>[26]</sup> reported that adding an Al-TCB master alloy to A356 increased the spiral flow length by approximately 35.4%, indicating a significant improvement in melt fluidity.

Recently, some studies have extended the use of grain refiners to the HPDC process, achieving improvements in microstructure and mechanical properties of die-cast Al-Si alloys<sup>[28, 29]</sup>. However, current research on TiB<sub>2</sub>in HPDC primarily focuses on its refining effect on primary  $\alpha$ -Al formed within the die cavity (( $\alpha$ -Al)<sub>II</sub>). In fact, the melt experiences two solidification stages with distinctly different cooling rates during HPDC: approximately 30-50 K/s in the shot sleeve and 100-200 K/s in the die cavity. The heterogeneous microstructure and defect of HPDC alloys forms through the coupling of solidification and flow in die cavity. TiB2 has the potential to influence solidification behavior during both the shot sleeve and cavity stages, allowing for regulation of ESCs formation in shot sleeve and solidification die cavity, thereby optimizing microstructure and minimizing defects in die castings. To date, the effects of Al-Ti-B on microstructure evolution, defect formation, and fluidity during long-distance melt flow in HPDC remain unclear and require further investigation.

In this work, a fluidity test mold with three channels of different thicknesses was employed to systematically investigate the evolution of microstructure and porosity along the filling distance in AlSi10MnMg alloy after the addition of TiB<sub>2</sub>, analyze the relationship between fluidity and solidification behavior, and provide a new perspective for optimizing the mechanical properties and flowability of HPDC Al-Si alloys.

#### 2 Experimental

#### 2.1 Materials and fabrication process

A commercial AlSi10MnMg alloy was used in this study. The melt was degassed at 750 °C by argon purging with rotary impeller stirring for 10 minutes. The Al-4Ti-2B master alloy containing TiB<sub>2</sub> particles was added to the melt at the 5th minute during degassing. Detailed information on the Al-4Ti-2B can be found in our previous work<sup>[30]</sup>. The addition levels of Al-4Ti-2B were 0%, 0.3%, and 0.6% (all compositions are in wt% unless

otherwise specified), and the corresponding alloys were designated as A0, A1, and A2. The chemical compositions of the alloys, measured using a spark direct-reading spectrometer, are listed in Table 1. Approximately 650 g of melt per shot was transferred to an LK-DCC 280T cold chamber die casting machine equipped with a vacuum system. The casting parameters were as follows: pouring temperature 700 °C, slow shot speed 0.2 m/s, fast shot speed 2 m/s, injection pressure 15 MPa, and mold temperature 120 °C. A spiral-shaped fluidity test mold containing three channels was employed to evaluate alloy fluidity, as illustrated in Fig. 1(a). The dimensions of the three channels were: L1 ( $10 \times 6 \times 1500 \text{ mm}$ ), L2 ( $8 \times 4 \times 1500 \text{ mm}$ ) 1500 mm), and L3 ( $10 \times 6 \times 1500$  mm). The flow length of each casting was used to assess the fluidity of the alloys. Casting trials were initiated after confirming mold temperature stabilization at 120 °C. The first 20 castings were discarded to ensure stability of castings. For each alloy composition, the average flow length was calculated based on 10 valid castings.

#### 2.2 Microstructure characterization

Samples for optical microstructure observation were sectioned at 500 mm from channels L1, L2, and L3. The L2 was selected as the representative to investigate the microstructural evolution along the flow path, with samples taken at 100 mm, 500 mm, 1000 mm, and 1500 mm, as shown in Fig. 1(a). All specimens were ground using silicon carbide papers and polished with diamond suspension, followed by observation using an optical microscope (OM, Zeiss, Axio Vert. A1). The area fraction of externally solidified crystals (ESCs) was quantified using ImageJ software. The sample at 500 mm in L2 was further examined using scanning electron microscopy (SEM, IT800-SHL, JEOL). For density measurements, specimens with dimensions of  $8 \times 4 \times 5 \text{ mm}^3$  were cut from L2 at 100 mm, 500 mm, 1000 mm, and 1500 mm. The density was measured using the Archimedes drainage method, and each sample was tested five times to obtain an average value.

Cylindrical samples ( $\Phi$ 3 × 5 mm) were taken from 500 mm and 1000 mm along the L2 runner for X-ray computed tomography (X-ray CT, Zeiss, Xradia 610 Versa), as shown in Fig. 1(b). The working voltage, current, and voxel size were set to 120 kV, 146  $\mu$ A, and 5 $\mu$ m, respectively. Dragonfly 3D software was used to reconstruct the 3D morphology of pores. The 3D equivalent diameter (DP) and sphericity (SP) of the pores were calculated using Eqs. (1) and (2), respectively.

$$D_P = \sqrt[3]{\frac{6V}{\pi}} \tag{1}$$

$$S_P = \frac{S}{V} \tag{2}$$

V and S represent the volume and surface area of individual pores, N is the number of pores within the analyzed volume, and  $V_0$  is the total volume of the analyzed region. The area fraction ( $f_{\rm ESCs}$ ) and equivalent diameter ( $d_{\rm eq}$ ) of externally solidified crystals (ESCs) were calculated using Eqs. (3) and (4), respectively.

$$f_{ESC} = \sum_{i=1}^{n} \frac{A}{A_0} \tag{3}$$

$$d_{eq} = 2\sqrt{\frac{A}{\pi}} \tag{4}$$

#### 2.3 Mechanical property tests

To analyze the evolution of mechanical properties along the filling path, tensile samples were taken from the L2 at 100 mm, 500 mm, and 1000 mm, as shown in Fig. 1(c). The specimens with dimensions shown in Fig. 1(c), were tested at room temperature using a universal material testing machine (SUNS, UTM-5105, P.R. China) under a constant crosshead speed of 2 mm/min. For each condition, at least five parallel samples were tested to ensure data reliability.

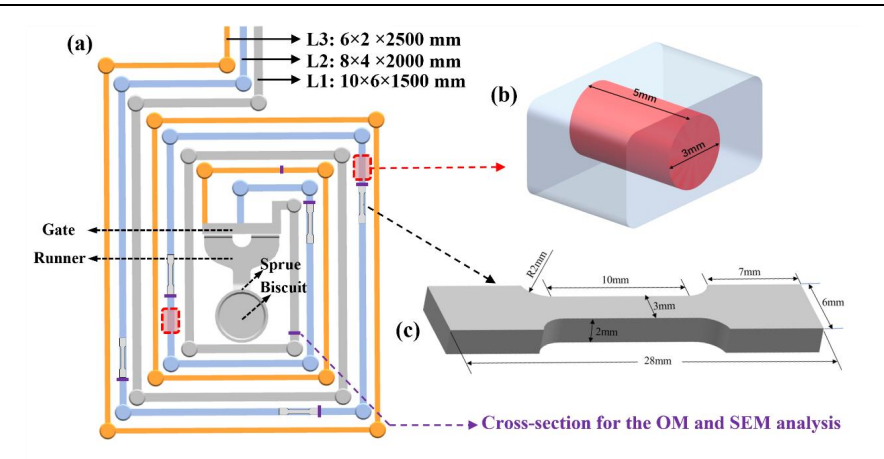


Fig. 1. (a) Configuration of casting and sampling position, (b) diagram of extracted CT sample, (c) dimension of tensile specimen

Table 1 the chemical composition of alloys in this work (wt%)

Tuble 1 the chemical composition of anoys in this work (we/n)								
Alloys	Si	Mn	Mg	Fe	Ti	В	Sr	Al
A0(AlSi10MnMg)	10.66	0.56	0.32	0.12	0.097	-	0.012	Bal.
A1(AlSi10MnMg+0.3% Al-4Ti-2B)	10.56	0.54	0.33	0.11	0.112	0.006	0.011	Bal.
A2(AlSi10MnMg+0.6% Al-4Ti-2B)	10.62	0.55	0.34	0.12	0.124	0.113	0.012	Bal.

#### 3 Result and discussion

#### 3.1 Microstructure under different section thickness

Typical SEM images and corresponding EDS elemental maps of the HPDC Al-Si alloy are presented in Fig. 2. Two morphologically distinct types of  $\alpha$ -Al grains can be clearly observed in the SEM images: coarse dendritic ESCs (yellow arrows) and fine secondary ( $\alpha$ -Al)<sub>II</sub> grains

(red arrows). The regions between  $\alpha$ -Al grains consist of coral-like eutectic structures (blue arrows) and blocky Fe-rich phases (orange arrows). The high cooling rate in the die cavity promotes the formation of blocky  $\alpha$ -Fe phases instead of the needle-like Fe-rich phases typically observed in conventional metal mold casting [31].

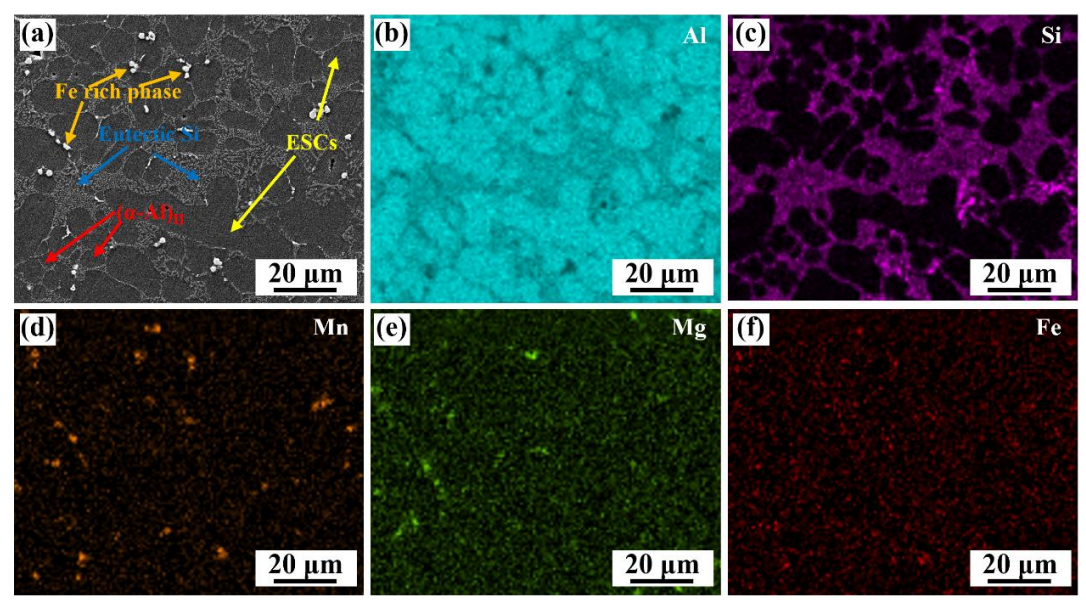


Fig. 2 (a) SEM map and corresponding element distribution maps based on EDS in500 mm of L2, (b) AI, (c) Si, (d) Mn, (e) Mg, (f) Fe.

Cross-sectional optical micrographs from surface to center across of L1, L2, and L3 are shown in Fig. 3(a–c), respectively. All three thickness conditions exhibit pronounced structural heterogeneity, with coarse ESCs concentrated at the center and fine  $(\alpha\text{-Al})_{II}$  along with eutectic Si dominating the surface. The distribution of area fraction of ESCs across the section for L1, L2, and L3 is presented in Fig. 3(d), showing an increasing trend from surface to center for all channels. This is attributed to the higher cooling rate at the surface, which promotes nucleation of  $(\alpha\text{-Al})_{II}$  and eutectic  $Si^{[32,\ 33]}$ , and the migration of ESCs toward the center driven by Magnus force under high-speed melt flow  $^{[34]}$ . A eutectic-rich band is observed between the surface and center, referred to as

eutectic band. This results from band accumulation of Si-rich residual liquid induced by rheological shearing of the solid-liquid mixture during filling<sup>[35]</sup>. Notably, the eutectic band width decreases with decreasing runner thickness. When the runner thickness was reduced from 6 mm (L1) to 2 mm (L3), the eutectic band width decreased from 1192 µm to 152 µm. This is because a thinner channel leads to a higher cooling rate in the die cavity, which accelerates nucleation of  $(\alpha-Al)_{II}$  and eutectic Si, increasing the solid fraction more rapidly. Consequently, the increased solid fraction imposes greater resistance to melt flow and shearing in the semi-solid region, reducing the accumulation zone of residual liquid and thus narrowing the eutectic band.

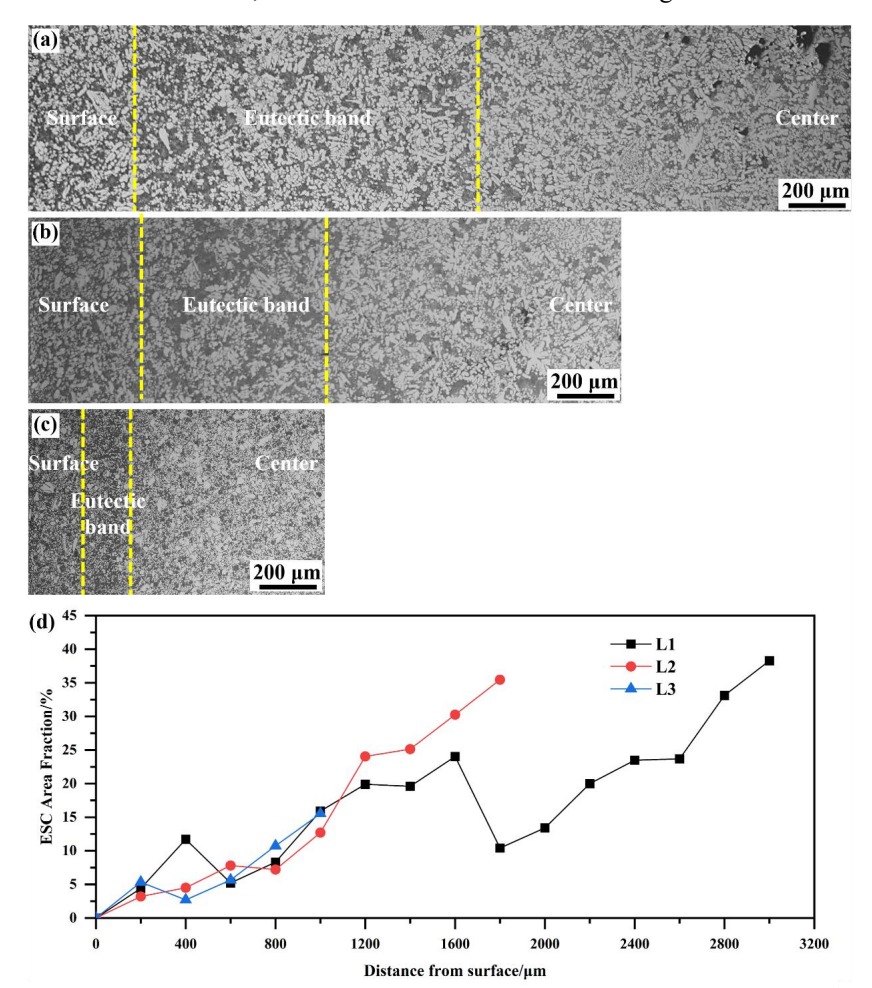


Fig. 3 Optical microstructures of the cross-section through surface to center at a flow distance of 500 mm: (a) L1, (b) L2, (c) L3. (d)

Distribution curves of area fractions of ESCs along the cross-section.

Microstructures at different positions in thickness (surface, eutectic band, center) for L1, L2, and L3 are shown in Fig. 4. It is evident that area fraction of ESCs and density decrease significantly with decreasing

thickness of channel across all regions. In L3, ESCs are barely visible at the surface. This is attributed to the higher shear force imposed by the melt in channel with greater cross-sectional changes, which intensifies the fragmentation of ESCs during flow [36]. Furthermore, the size of  $(\alpha$ -Al) $_{II}$  grains also decreases markedly with

decreasing runner thickness, due to the enhanced nucleation driven by higher cooling rates<sup>[37]</sup>.

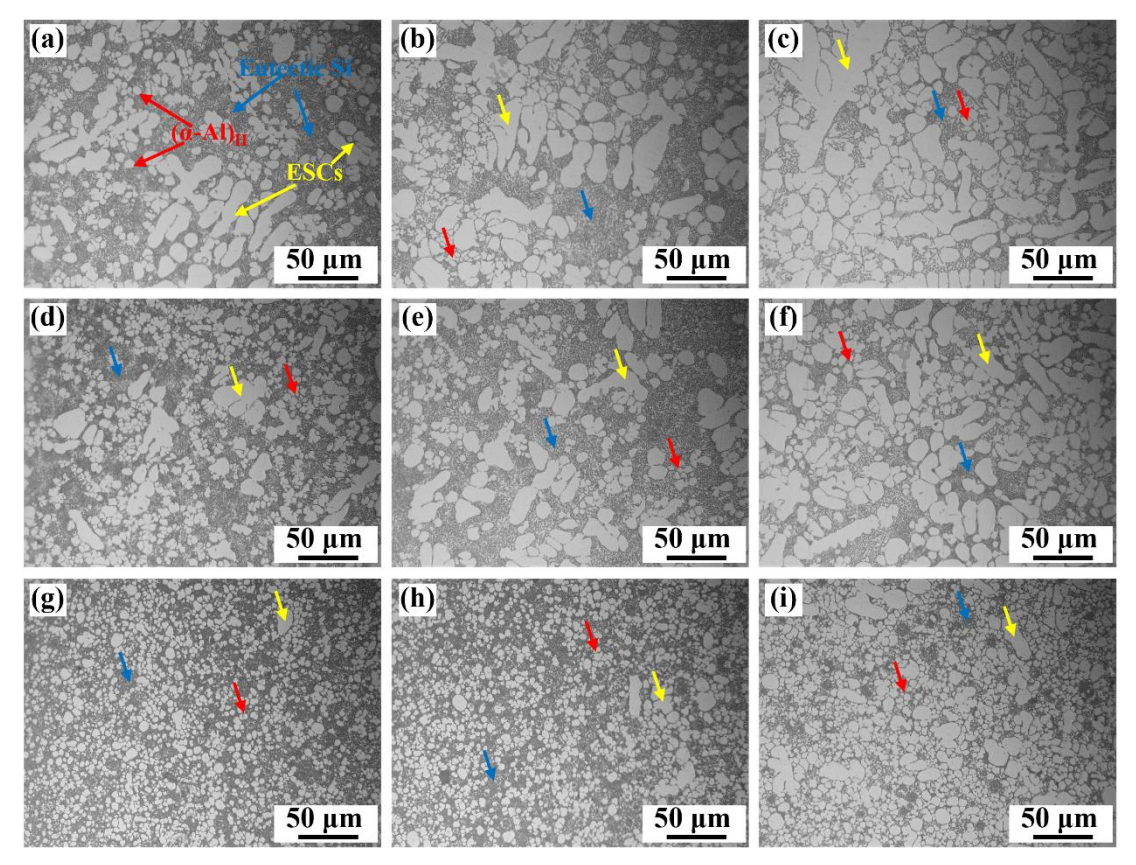


Fig. 4 Optical microstructures of L1 (a) - (c), L2 (d) - (f) and L3 (g) - (i) at different locations in the cross-section, (a), (d) and (g) are at the surface, (b), (e) and (h) at the eutectic band, (c), (f) and (i) at the center.

## 3.2 The effect of TiB2 on ESCs and porosity along filling distance

The L2 was selected as a representative to analyze the microstructural evolution with increasing filling distance. Fig. 5 shows the microstructure at the center of L2 for different TiB2 addition levels along various filling distances. Specifically, Fig. 5(a-d) corresponds to A0, Fig. 5(e-h) to A1, and Fig. 5(i-l) to A2. As shown in Fig. 6(a), the area fraction of ESCs declines as the filling distance increases, and their average diameter also decreases, as illustrated in Fig. 6(b). On one hand, in the shot sleeve, heat dissipation primarily occurs through the sleeve wall and plunger, resulting in a temperature gradient where the melt temperature increases with distance from the plunger. This leads to reduced ESC formation and growth with increasing distance. On the other hand, the lower velocity of ESCs compared to the liquid phase during high-speed melt flow<sup>[12]</sup> also contributes to their decreasing content

along the flow direction. Moreover, the density of A0 decreases with increasing filling distance, which indicates increasing porosity. After TiB2 addition, both the area fraction and size of ESCs decreased, while alloy density increased, as shown in Fig. 6(a-c). Notably, the reduction in area fraction and size of ESCs was more pronounced in A1 than in A2, indicating that excessive TiB2 addition (i.e., 0.6%) leads to increased ESC content in the casting. Interestingly, when the filling distance was below 1000 mm, the density of A2 was higher than A1; however, beyond 1000 mm, A2 exhibited a lower density than A1. Our previous work[30] indicated that the filling behavior in the die cavity is governed not only by ESCs but also by solidification dynamics. While TiB2 addition increases the amount of ESCs entering the cavity, it also improves the uniformity of shear deformation and reduces porosity formation. When the filling distance is less than 1000 mm, the pressure transmitted from the plunger to the melt is

sufficient, allowing TiB<sub>2</sub>-induced optimization of solidification in die cavity to dominate, resulting in higher density in A2 despite its higher ESC content compared to A1. However, at distances beyond 1000 mm, the reduced

plunger pressure leads to the ESCs obstruction of fluid flow to dominate, thereby reducing the density of A2 relative to A1.

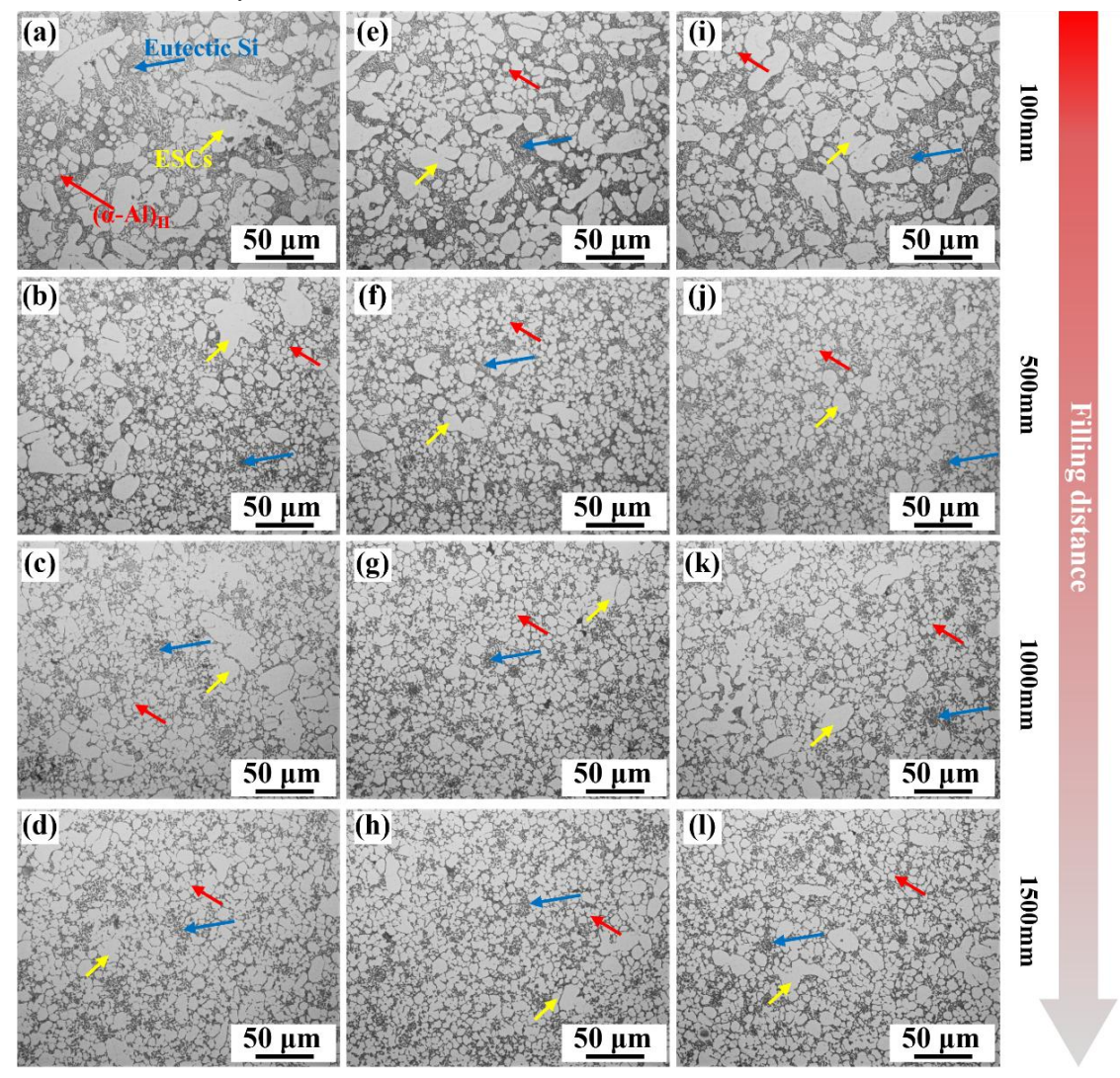


Fig. 5 Optical microstructures of different alloys along the flow distance: (a)-(d) A0, (e)-(h) A1, (i)-(l) A2. (a), (e), (i) are at 100 mm, (b), (f), (j) are at 100 mm, (c), (g), (k) are at 100 mm, (d), (h), (l) are at 100 mm.

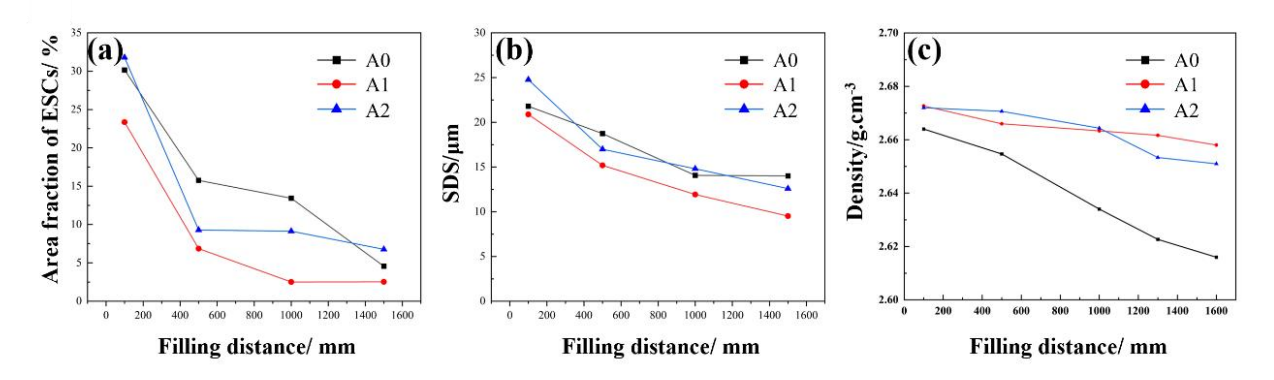


Fig. 6 Statistics of (a) area fraction of ESCs, (b) secondary dendrite spacing (SDS), and (c) density along the flow distance in L2.

The mechanism by which TiB<sub>2</sub> affects formation of ESCs in the shot sleeve is illustrated in Fig. 7. Without TiB<sub>2</sub>, heat loss through the sleeve wall induces a radial temperature gradient, promoting (α-Al)<sub>II</sub> nucleation near the wall, as shown in Fig. 7(a). Under these conditions, ESCs nucleate and grow mainly near the sleeve wall, governed by thermal gradients. Simulations using ProCAST are shown in Fig. 7(d) and the results indicate that the melt velocity increases from the sleeve wall towards the center. According to the Magnus effect [34], solid particles in the melt experience a force directing them toward the center, promoting their migration (Fig. 7(c) and (e)). As the central melt has a higher temperature and velocity, ESCs that migrate from the wall toward the center are likely to undergo remelting and fragmentation.

When TiB2 is added, it reduces the critical undercooling needed for α-Al nucleation, allowing ESCs to nucleate farther from the sleeve wall and weakening the dependence on the thermal gradient. As a result, more ESCs float freely in the melt. During high-velocity flow, more ESCs migrate toward the center, where remelting and fragmentation are more intense, ultimately reducing the size and content of ESCs entering the cavity, as shown in A1 (Fig. 7(f)). However, with further TiB2 addition (A2), the number of floating ESCs increases, and a balance eventually reached **ESC** between fragmentation/remelting and their transport toward the center, resulting in a net increase in ESCs entering the cavity. Thus, an optimal TiB2 content of 0.3 wt% is identified.

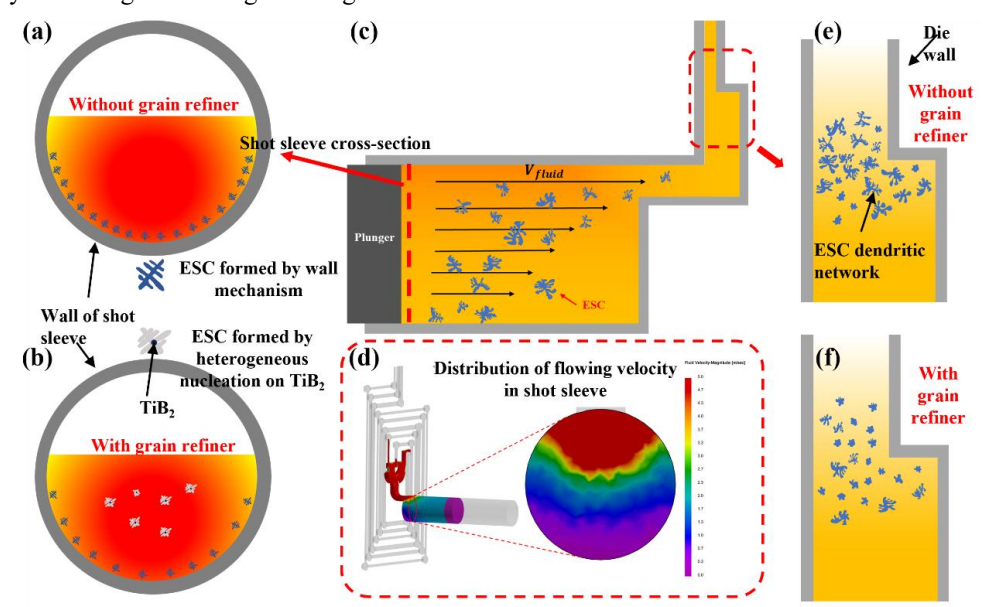


Fig. 7 The schematic diagram of the mechanism for evolution of ESCs.

The 3D reconstructed morphologies of porosity at 500 mm and 1000 mm along L2 are shown in Fig. 8. As the filling distance increases from 500 mm to 1000 mm, the porosity volume fraction in A0 increases from 21.09% to 48.80%, while in A1 it rises from 14.88% to 21.69%. This increase is consistent with the density reduction trend shown in Fig. 6(c). Addition of TiB<sub>2</sub> significantly reduces the porosity volume fraction at both locations. Scatter plots of sphericity versus equivalent diameter of porosity are shown in Fig. 8(e)–(h). A greater number of data points appear in the lower-right region (larger, irregular

pores) at 1000 mm compared to 500 mm in both A0 and A1, indicating increased formation of large pores with increasing flow distance. Addition of TiB<sub>2</sub> causes a leftward shift in both scatter plots, reflecting a reduction in large pore size. As demonstrated in Fig. 6, addition of 0.3 % TiB<sub>2</sub> effectively reduces ESC content in the casting. According to Dahle et al.[15], the resistance of semi-solid slurries to shear deformation increases with solid fraction and grain size. Therefore, the reduction in large ESCs dendrites facilitates local particle migration and rotation, enhancing melt flow and reducing porosity formation.

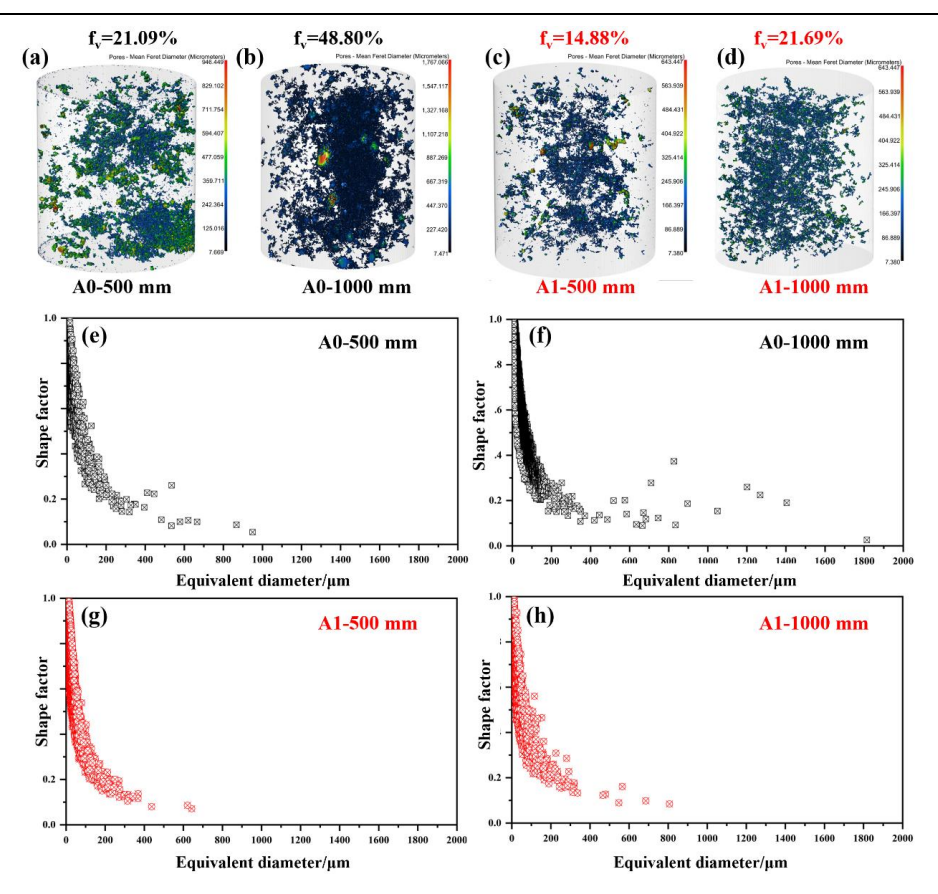


Fig. 8 3D reconstruction of pores: (a)-(b) A0, (c)-(d) A1, (a) and (c) are at 500 mm of L2, (b) and (d) are at 1000 mm of L2, and (e)-(h) are correspondingly scatter plots of the shape factor versus equivalent diameter.

### 3.3 The effect of TiB2 on fluidity and mechanical properties

The actual castings of A0, A1, and A2 are shown in Fig. 9(a)-(c), and the corresponding measured flow lengths in L1, L2, and L3 are summarized in Fig. 9(d). In the thickest runner (L1), all three alloys completely filled the mold cavity, making it unsuitable for evaluating flowability differences. In L2, the flow lengths for A0, A1, and A2 were 1700  $\pm$  21.2  $\mu m,~1833.3~\pm~59.1~\mu m,$  and  $1796.9 \pm 24.9 \, \mu m$ , respectively. In L3, the values were  $648.8 \pm 13.4 \ \mu m,\ 740 \pm 42.4 \ \mu m,\ and\ 746 \pm 12.5 \ \mu m,$ respectively. These results indicate that the addition of TiB<sub>2</sub> significantly improves the alloy's fluidity, with the 0.3 % Al-4Ti-2B addition (A1) performing better than the 0.6 % addition (A2). The driving force for melt filling in the die cavity is the pressure transmitted by the plunger to the liquid phase. As the solid fraction increases, the resistance to melt flow rises accordingly [14], leading to a pressure drop in the interdendritic liquid. When this pressure drop approaches the driving pressure, flow ceases. Han et al.[38]reported that the presence of ESCs accelerates the pressure drop, thereby hindering liquid phase filling and deteriorating alloy fluidity. Since the addition of TiB2 effectively reduces the ESCs content in

the castings, it helps to improve fluidity.

The ultimate tensile strength (UTS), yield strength (YS), and elongation of the alloys at different filling distances are presented in Fig. 9(e), (f), and (g), respectively. Notably, when the filling distance exceeded 1000 mm, all three alloys—A0, A1, and A2—exhibited a significant deterioration in mechanical performance. For example, the UTS of A0 decreased from 241 MPa at 100 mm to 192 MPa at 1500 mm, while the elongation dropped from 3.5% to 1.8%. This degradation is mainly attributed to the increase in large porosity at the far end of the cavity due to poor filling. Both A1 and A2 exhibited higher UTS, YS, and elongation compared to A0, indicating that the addition of TiB2 improves the mechanical performance of the alloy. This improvement is primarily due to the reduction of ESCs and porosity in the castings induced by TiB2 addition.

Interestingly, for filling distances less than 1000 mm, A2 exhibited higher elongation than A1. However, when the filling distance exceeded 1000 mm, elongation of A2 became lower than that of A1. This trend is closely related to porosity evolution. As shown in Fig. 6(c), A2 exhibited higher density than A1 at filling distances below 1000 mm, indicating lower porosity content;

whereas at distances beyond 1000 mm, density of A2 dropped below that of A1, reflecting increased porosity

and thus reduced ductility.

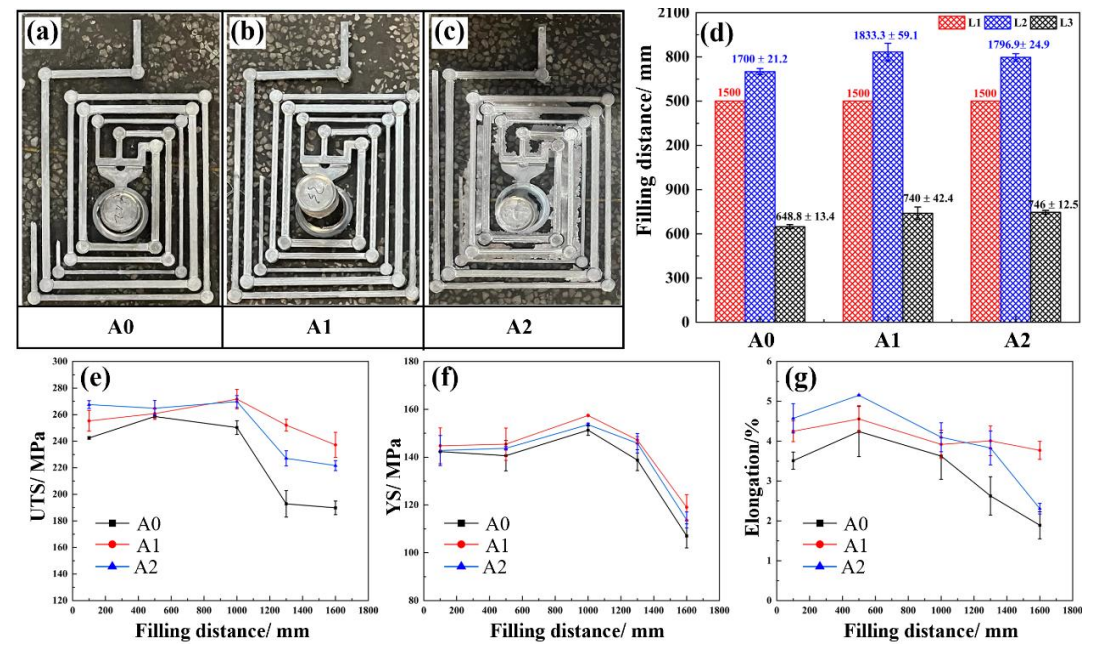


Fig. 9 Castings of different alloys: (a) A0, (b) A1, (c) A2 and (d) filling distance of A0, A1 and A2. (e) UTS, (f) YS, and (g) Elongation at different flow distances in L2.

The fracture morphologies of A0 and A1 are shown in Fig. 10. As observed in Fig. 10(a) and (d), the surface of the of fracture A1 exhibits significantly fewer gas pores and shrinkage defects compared to A0. At the fracture center, both A0 and A1 display large shrinkage clusters, which are attributed to insufficient feeding in the final solidification zone. However, the size of the shrinkage region in A1 (Fig. 10(e)) is notably smaller than that in A0 (Fig. 10(b)). ESCs were observed

surrounding the shrinkage cavities, as shown in Fig. 10(c), indicating that the presence of ESCs impedes melt flow, promoting shrinkage formation. These coarse shrinkage pores serve as crack initiation sites and facilitate crack propagation, thereby degrading the mechanical performance of the alloy. The addition of TiB<sub>2</sub> effectively reduces porosity, thus contributing to improved mechanical properties.

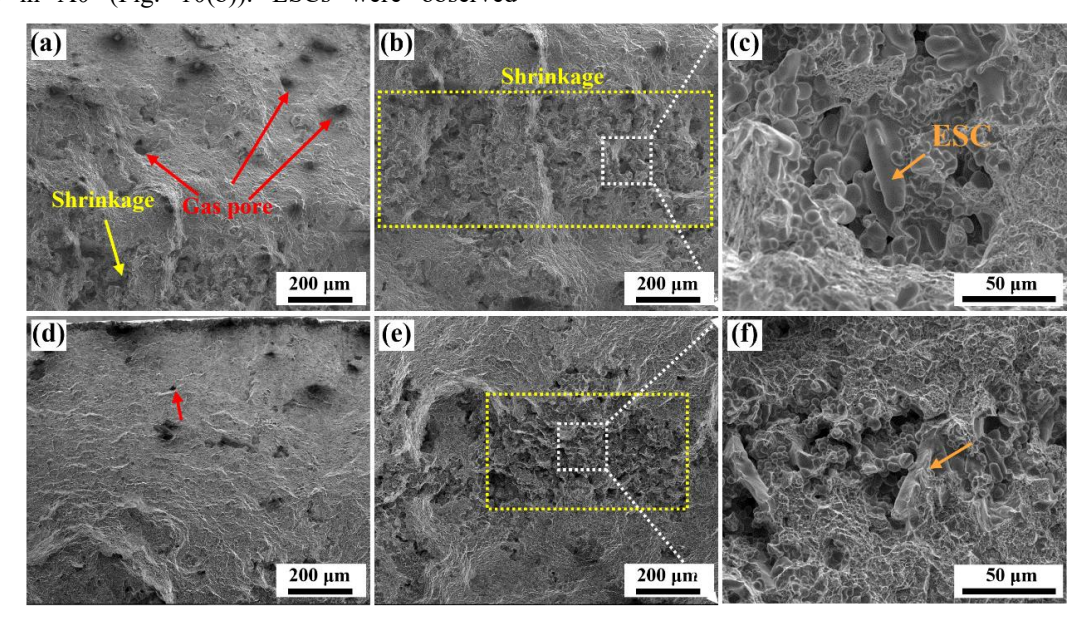


Fig. 10 Fracture morphology of (a)-(c) A0 and (b)-(c) A1, (a) and (d) are surface and (b) and (e) are center, (c) and (f) are enlarged images of the regions in (b) and (e), respectively.

#### **5 Conclusions**

In this study, long-distance fluidity test castings of AlSi10MnMg alloy were produced via high-pressure die casting (HPDC), and the effects of TiB<sub>2</sub> on microstructure, mechanical properties, and fluidity at various filling distances were systematically investigated. Based on the experimental results and analyses, the following conclusions can be drawn:

- (1) The microstructure varied significantly with thickness of channel. When the thickness of channel decreased from 6 mm to 2 mm, the area fraction of ESCs and the width of the eutectic band at a flow distance of 500 mm decreased from 12% and 1192  $\mu$ m to 2% and 152  $\mu$ m, respectively.
- (2) With increasing filling distance, the content of ESCs and porosity in the castings decreased, accompanied by a reduction in density. The addition of Al-4Ti-2B effectively reduced the area fraction and size of ESCs, as well as the volume fraction and size of pores. The alloy with 0.3 wt.% addition (A1) exhibited lower ESC area fraction and smaller ESC size compared to the 0.6 wt.% alloy (A2). For filling distances below 1000 mm, A1 showed lower density than A2, whereas for distances above 1000 mm, A1 exhibited higher density.
- (3) As the filling distance increased up to 1000 mm, the mechanical properties of the castings deteriorated significantly. The addition of 0.3 wt.% and 0.6 wt.% Al-4Ti-2B increased the flow length in L2 from 1700 mm to 1833 mm and 1796.9 mm, respectively. With 0.3 wt.% Al-4Ti-2B, the UTS, YS, and elongation at a filling distance of 1500 mm improved from 190.1 MPa, 137 MPa, and 1.9% to 249.3 MPa, 144.5 MPa, and 4.0%, respectively. For distances below 1000 mm, A1 exhibited lower UTS and elongation than A2, while for distances above 1000 mm, A1 showed superior tensile performance compared to A2.

#### Credit authorship contribution statement

Lei Liu: Writing – original draft, Methodology, Investigation, Conceptualization. Weixiao Yang: Visualization, Validation. Kai Zhao: Investigation, Formal analysis. Yanqiang Li: Methodology, Investigation. Tao Zhang: Resources, Methodology. Ying Fu: Resources, Methodology. Zhirou Zhang: Methodology, review, editing. Enyu Guo: Methodology, Funding acquisition. Huijun Kang: Methodology, Funding acquisition. Zongning Chen: Writing – review & editing, Supervision, Funding acquisition, Conceptualization. Tongmin Wang:

Project administration, Funding acquisition.

#### Acknowledgements

This work was supported by the National Key Research and Development Program of China (No. 2021YEA1600702), the Natural Science Foundation of Guangxi (ZY24212052), the National Natural Science Foundation of China (Nos. 52174356, U24A2028 and U22A20174), the Major Science and Technology Projects of Longmen Laboratory (No.231100220400), the Fundamental Research Funds for the Central Universities and the Natural Science Foundation of Ningbo (No.2022J010).

#### References

- [1] Xiao R, Wang J, Meng S, et al. Simulation study on integrated bottom car body formation by high pressure die casting with a dual injection system. China Foundry, 2025.
- [2] Zhu H, Xia C, Zhang H, et al. Design of Non-Heat Treatable High Pressure Die Casting Al Alloys: A Review. Journal of Materials Engineering and Performance, 2024, 33(17): 8601-8626.
- [3] Niu X P, Hu B H, Pinwill I, et al. Vacuum assisted high pressure die casting of aluminium alloys. Journal of Materials Processing Technology, 2000, 105(1): 119-127.
- [4] Dong X, Youssef H, Zhu X, et al. High as-cast strength die-cast AlSi9Cu2Mg alloy prepared by nanoparticle strengthening with industrially acceptable ductility. Journal of Alloys and Compounds, 2021, 852: 156873.
- [5] Baser T A, Umay E, Akıncı V New Trends in Aluminum Die Casting Alloys for Automotive Applications. The Eurasia Proceedings of Science Technology Engineering and Mathematics, 2022, 21: 79-87.
- [6] Otarawanna S, Gourlay C M, Laukli H I, et al. Formation of the surface layer in hypoeutectic Al-alloy high-pressure die castings. Materials Chemistry and Physics, 2011, 130(1): 251-258.
- [7] Otarawanna S, Gourlay C M, Laukli H I, et al. Microstructure formation in high pressure die casting. Transactions of the Indian Institute of Metals, 2009, 62(4): 499-503.
- [8] Liu F, Zhao H, Chen B, et al. Investigation on microstructure heterogeneity of the HPDC AlSiMgMnCu alloy through 3D electron microscopy. Materials & Design, 2022, 218: 110679.
- [9] Liu R, Zheng J, Godlewski L, et al. Influence of pore characteristics and eutectic particles on the tensile properties of Al–Si–Mn–Mg high pressure die casting alloy.

- Materials Science and Engineering: A, 2020, 783: 139280.
- [10] Yang Y, Huang S, Zheng J, et al. Effect of porosity and α-Al(Fe/Mn)Si phase on ductility of high-pressure die-casting Al-7Si-0.2Mg alloy. Transactions of Nonferrous Metals Society of China, 2024, 34(2): 378-391.
- [11] Jiao X Y, Wang P Y, Liu Y X, et al. Fracture behavior of a high pressure die casting AlSi10MnMg alloy with varied porosity levels. Journal of Materials Research and Technology, 2023, 25: 1129-1140.
- [12] Fu J, Zheng H, Guo L, et al. Microstructure, eutectic Si distribution, and mechanical properties of Al-6Si-Mg high pressure die castings with long mold filling distance. Journal of Manufacturing Processes, 2025, 150: 391-406.
- [13] Han Q A Model correlating fluidity to alloy variables in hypoeutectic alloys. Acta Materialia, 2022, 226: 117587.
- [14] Gourlay C M, Dahle A K, Nagira T, et al. Granular deformation mechanisms in semi-solid alloys. Acta Materialia, 2011, 59(12): 4933-4943.
- [15] Dahle A K, StJohn D H Rheological behaviour of the mushy zone and its effect on the formation of casting defects during solidification. Acta Materialia, 1998, 47(1): 31-41.
- [16] Guo L, Zheng H, Wang X, et al. Effect of vanadium on Fe-rich intermetallics in HVDC Al-8Si-0.2Mg-0.3Fe alloys. Materials Today Communications, 2025, 46: 112664.
- [17] Jiang Y, Zheng H, Liu F, et al. Effect of Zn Addition on the Microstructural Heterogeneity and Mechanical Properties of Vacuum-Assisted High-Pressure Die Casting Al-Si-Mg-Cu alloys. Advanced Engineering Materials, 2023, 25(9): 2201457.
- [18] Li J, Yu W, Sun Z, et al. Influence of introducing Zr, Ti, Nb and Ce elements on externally solidified crystals and mechanical properties of high-pressure die-casting Al–Si alloy. International Journal of Minerals, Metallurgy and Materials, 2025, 32(1): 147-153.
- [19] Liu W, Zhang W, Wang P, et al. Effect of slow shot speed on externally solidified crystal, porosity and tensile property in a newly developed high-pressure die-cast Al-Si alloy. China Foundry, 2024, 21(1): 11-19.
- [20] Jiao X Y, Zhang Y F, Wang J, et al. Characterization of externally solidified crystals in a high-pressure die-cast AlSi10MnMg alloy and their effect on porosities and mechanical properties. Journal of Materials Processing Technology, 2021, 298: 117299.
- [21] Niu Z, Liu G, Li T, et al. Effect of high pressure die casting on the castability, defects and mechanical properties of aluminium alloys in extra-large thin-wall castings. Journal of Materials Processing Technology, 2022, 303: 117525.
- [22] Dong X, Zhu X, Ji S Effect of super vacuum assisted high

- pressure die casting on the repeatability of mechanical properties of Al-Si-Mg-Mn die-cast alloys. Journal of Materials Processing Technology, 2019, 266: 105-113.
- [23] Trometer N, Godlewski L A, Prabhu E, et al. Effect of Vacuum on Die Filling in High Pressure Die Casting: Water Analog, Process Simulation and Casting Validation. International Journal of Metalcasting, 2024, 18(1): 69-85.
- [24] Li J, Hage F S, Ramasse Q M, et al. The nucleation sequence of α-Al on TiB2 particles in Al-Cu alloys. Acta Materialia, 2021, 206: 116652.
- [25] Sigworth G K Grain Refinement of Al-Si-Cu Alloys by AlB2 and (Al,Ti)B2. International Journal of Metalcasting, 2024.
- [26] Zhao Z, Li D, Yan X, et al. Insights into the dual effects of Ti on the grain refinement and mechanical properties of hypoeutectic Al–Si alloys. Journal of Materials Science & Technology, 2024, 189: 44-59.
- [27] Dahle A K, Tøndel P A, Paradies C J, et al. Effect of grain refinement on the fluidity of two commercial Al-Si foundry alloys. Metallurgical and Materials Transactions A, 1996, 27(8): 2305-2313.
- [28] Hu C, Zhu H, Wang Y, et al. Microstructure features and mechanical properties of non-heat treated HPDC Al9Si0.6Mn–TiB2 alloys. Journal of Materials Research and Technology, 2023, 27: 2117-2131.
- [29] Dong X, Youssef H, Zhang Y, et al. High performance Al/TiB2 composites fabricated by nanoparticle reinforcement and cutting-edge super vacuum assisted die casting process. Composites Part B: Engineering, 2019, 177: 107453.
- [30] Liu L, Yang W, Zhao K, et al. The effects of TiB2 on segregation bands, porosities and mechanical properties of hypoeutectic AlSi alloys by high pressure die-casting. Materials Characterization, 2025, 221: 114741.
- [31] Xiang K, Qin L, Zhao Y, et al. Operando study of the dynamic evolution of multiple Fe-rich intermetallics of an Al recycled alloy in solidification by synchrotron X-ray and machine learning. Acta Materialia, 2024, 279: 120267.
- [32] Zheng H, Jiang Y, Liu F, et al. Microstructure heterogeneity optimization of HPDC Al-Si-Mg-Cu alloys by modifying the characteristic of externally solidified crystals. Journal of Alloys and Compounds, 2024, 976: 173167.
- [33] Niu G, Wang J, Li J, et al. The formation mechanism of the chill fine-grain layer with high supersaturation and its influence on the mechanical properties of die casting Al-7Si-0.5Mg alloy. Materials Science and Engineering: A, 2022, 833: 142544.
- [34] Zhang X, Zhou Y, Ezawa M Magnetic bilayer-skyrmions without skyrmion Hall effect. Nature Communications,

2016, 7(1): 10293.

- [35] Gourlay C M, Dahle A K Dilatant shear bands in solidifying metals. Nature, 2007, 445(7123): 70-73.
- [36] Li X, Yu W, Wang J, et al. Influence of melt flow in the gating system on microstructure and mechanical properties of high pressure die casting AZ91D magnesium alloy. Materials Science and Engineering: A, 2018, 736: 219-227.
- [37] Lu B, Yu W, Li Y, et al. Formation of banded intergranular
- segregation and control via micro-alloying in twin-roll casted Al–Zn–Mg–Cu alloy with high solidification interval. Materialia, 2022, 22: 101406.
- [38] Han Q, Zhang J Fluidity of Alloys Under High-Pressure Die Casting Conditions: Flow-Choking Mechanisms. Metallurgical and Materials Transactions B, 2020, 51(4): 1795-1804.